# Thermochemical convection and helium concentrations in mantle plumes

Henri Samuel *, Cinzia G. Farnetani

*Laboratoire de Dynamique des Systèmes Géologiques, Institut de Physique du Globe de Paris, Paris, France*

## Abstract

Compositionally heterogeneous material may exist in the lowermost mantle [van der Hilst and Kárason, Science 283 (1999) 1885–1888]. Here we use a numerical model to investigate the dynamics of (i) the subducted oceanic crust and lithosphere, (ii) a deep layer chemically denser, relatively undegassed and enriched in radiogenic elements. Tracers carry U, Th, K, and He concentrations which vary due to radioactive decay and to partial melting and degassing processes. We investigate the stability of the denser layer and find that by considering a depth dependent thermal expansion coefficient and temperature dependent viscosity, a layer with a chemical density excess of 2.4% can remain stable and poorly mixed until present-day time. The calculated helium ratios are in good agreement with $^3$He/$^4$He observed at ridges and hotspots and show that the large spectrum of helium ratios of OIB can be explained by mixing between undegassed material, recycled oceanic crust and lithosphere. For MORB, the sharp spectrum of helium ratios may be due to a degassed, homogeneous and well mixed shallow mantle.
© 2002 Elsevier Science B.V. All rights reserved.

*Keywords:* helium; mantle; thermochemical convection

## 1. Introduction

Purely thermal convection models have significantly improved our understanding of mantle dynamics and explain some important geophysical observations [1]. However, thermal convection fails to explain other first-order seismological and geochemical observations, which instead support the existence of chemical heterogeneities in the Earth's mantle. Recent tomographic models display large-scale slow velocity domains in the lower mantle under Africa and the Pacific (e.g. [2] and references therein). Their large negative velocity anomaly, their shape and size, and the observed normal mode-splitting [3] are inconsistent with a purely thermal origin. 'Superplumes' instead arise naturally in thermochemical convection simulations [4], since the compositionally denser material tends to pile beneath upwellings. Fluid dynamics laboratory experiments of miscible viscous fluids with different densities [5] show the formation of large, vertically oscillating, domes and that the convection regime is affected even by relatively low compositional density excess. Other seismological observations [6,7] indi-

* Corresponding author. Tel.: +33-1-44-27-22-38;
Fax: +33-1-44-27-24-81.
*E-mail address:* samuel@ipgp.jussieu.fr (H. Samuel).

cate that the lowermost mantle (i.e. roughly 300 km above the core–mantle boundary, CMB) is more heterogeneous than previously thought and suggest the presence of chemical heterogeneities. Van der Hilst and Kárason [8] proposed that the compositional heterogeneous region may extend up to 1000 km above the CMB.

Another major unresolved issue by purely thermal convection models is the well known geochemical difference between depleted mid-ocean ridge basalts (MORB) and enriched ocean island basalts (OIB) (see [9] and references therein). Mantle convection would efficiently stir the geochemical heterogeneities on relatively short time scales [10,11] and even models that include physical parameters inhibiting stirring fail to explain the different helium ratios between MORB and OIB [12]. Therefore, a fundamental question is how geochemical heterogeneities can persist in a vigorously convecting mantle for billions of years, as required by geochemical observations. The subduction of oceanic crust and lithosphere introduces heterogeneous material in the mantle. By modeling the dynamics and the geochemical evolution of the denser subducted crust, Christensen and Hofmann [13] find that less than 20% of the eclogitic crust accumulates in the D″ region for a time period long enough to develop an 'enriched' isotopic signature (for U–Pb and Sm–Nd systems) which reproduces the geochemical difference between MORB and HIMU-type OIB. Using a time dependent box model Coltice and Ricard [14] study the Rb–Sr and U–Pb–He systems and propose that the high helium ratio in plumes is due to a low concentration of $^4$He, induced by low U and Th in the source region. We remark that this model is based on several crucial assumptions which have not been tested dynamically. Their interpretation is in contrast with the idea that high $^3$He/$^4$He are due to relatively undegassed material with high $^3$He/(U+Th). The existence of relatively undegassed material with high Ne$_{solar}$/(U+Th) is supported by near-solar neon isotopic ratios observed at Loihi [15] and Iceland [16,17]. Albarède [18] investigates the U–Th–He and K–Ar systems using a time dependent box model and concludes that whole mantle convection is compatible with the isotopic evidence provided

by rare gases. However, his calculated present-day concentrations of U and Th in the upper mantle are, respectively, five times and eight times greater than the maximum values for the MORB's source estimated by Jochum et al. [19]. Clearly, the concentrations and the distribution of radiogenic elements are of central importance for understanding mantle structure and evolution. The relatively low concentration of U and Th in the depleted mantle source of MORB cannot be extrapolated to the whole mantle, since the estimated internal heat production is inconsistent with the measured heat flux at the Earth's surface. This discrepancy requires the existence of a 'hidden reservoir', enriched in heat producing elements [20]. Constraints imposed by the U–Th systematics indicate that a substantial fraction of the mantle should have near-primitive value of the Th/U ratio [21]. This supports the model by Kellogg et al. [22], which proposes the existence of a chemically denser reservoir in the deep mantle, enriched in radiogenic elements and in primordial gases.

In this paper we investigate the dynamics and the geochemical implications of a denser, relatively primitive and poorly degassed layer in the lower mantle. We use a convection model with active tracers to follow the evolution of the denser reservoir and of the subducted crust and lithosphere. Each tracer carries the concentrations of U, Th, K, $^4$He and $^3$He, which vary with time owing to the radioactive decay and to partial melting and degassing. This allows us (1) to have a heterogeneous and time dependent internal heat production, associated with the local concentration of radiogenic elements, (2) to calculate the helium ratios for partial melts formed at spreading ridges and at hotspots, (3) to consider a fully dynamical model, where surface velocities are not imposed as boundary conditions. We first investigate the stability of the layer, by varying systematically several physical parameters. We then analyze in detail a plausible case in which the denser layer remains stable until present-day time, with a compositional density excess of 2.4% with respect to the reference density, and with an initial volume corresponding to 25% of the whole mantle. The results on helium ratios are compared with observations.

## 2. Numerical method

### 2.1. The finite element model

We use the two-dimensional finite element model ConMan [23] in Cartesian geometry to simulate solid state convection for a Newtonian, incompressible viscous fluid at infinite Prandtl number. Active tracers are used to model the effect of density heterogeneities and of a heterogeneous distribution of heat producing elements. This Lagrangian formalism is more reliable than the Eulerian formalism of a chemical field, since it does not suffer from numerical diffusion [24]. The non-dimensional equations for thermochemical convection with the Boussinesq approximation are:
conservation of mass:

$$\nabla \cdot U = 0, \tag{1}$$

conservation of momentum:

$$-\nabla p + \nabla \cdot \sigma - Ra[\theta - B\chi]\vec{z} = 0, \tag{2}$$

conservation of energy:

$$\frac{\partial \theta}{\partial t} + U \cdot \nabla \theta = \Delta \theta + H, \tag{3}$$

where $U$ is the velocity vector, $\theta$ the potential temperature, $t$ is time, $p$ the dynamic pressure, $\sigma = \eta(\theta)(U_{i,j} + U_{j,i})$ is the deviatoric stress, $\eta(\theta)$ the dynamic viscosity, $H$ the internal heating, and $\vec{z}$ is a unit vector in the vertical direction. The equations are non-dimensionalized by scaling distance over the depth of the box $D = 2900$ km; temperature according to the temperature contrast between the top and the bottom surface $\Delta\theta = 3000$ K; time according to $D^2/\kappa$, the thermal diffusivity $\kappa = 10^{-6}$ m$^2$ s$^{-1}$; the internal heating $H$ is scaled over $\rho_0 D^2/k\Delta\theta$, where $\rho_0 = 4155$ kg m$^{-3}$ is the reference mantle density and $k = 4.8$ W m$^{-1}$ K$^{-1}$ is the thermal conductivity. The Rayleigh number for a purely bottom heated case is:

$$Ra = \frac{g\alpha_0 \Delta\theta \rho_0 D^3}{\kappa \eta_0}, \tag{4}$$

while for models with bottom and internal heating the effective Rayleigh number is [25]: $Ra_{ef} = Ra(1 - (r/2))$, where $r$ is the ratio of the internal heat flux over the total heat flux. The buoy-ancy number $B$ is the chemical density contrast over the thermal density contrast:

$$B = \frac{\Delta\rho_c}{\rho_0 \alpha_0 \Delta\theta}. \tag{5}$$

$\chi$ expresses the composition of the fluid in chemical heterogeneities and ranges between 0 and 1. $\chi$ depends on the local volumic fraction of crust, lithosphere and denser undegassed material. Its calculation will be explained in detail in Section 2.2. The equation of state for density is thus:

$$\rho = \rho_0(1 - \alpha_0 \Delta\theta + \beta\chi), \tag{6}$$

where $\beta$ represents the relation between the compositional heterogeneity and the associated chemical density anomaly: $\beta = (1/\rho_0)(\partial\rho/\partial\chi)|_{\theta=0}$.

Mantle viscosity can be constant or temperature dependent according to:

$$\eta(\theta) = \eta_0 \exp[-A(\theta - 0.5)], \tag{7}$$

where $\eta_0 = 10^{22}$ Pa s and $A$ is a constant chosen to give a maximum viscosity contrast of two orders of magnitude. A viscosity jump of one order of magnitude is imposed between upper and lower mantle.

The thermal expansion coefficient can be constant or depth dependent according to the exponential law [13]:

$$\alpha(z) = \frac{\alpha_0 d}{1 - e^{-d}} e^{-d(1-z)}, \tag{8}$$

where $\alpha_0 = 2 \times 10^{-5}$ K$^{-1}$ is the mean value of the thermal expansion coefficient and the constant $d$ controls the variation with depth. In such case, $Ra$ and $B$ in Eq. 2 have to be multiplied by a factor $\alpha(z)/\alpha_0$ and $\alpha_0/\alpha(z)$, respectively. High pressure experiments [26] have estimated that $\alpha$ ranges between 4 and $5 \times 10^{-5}$ K$^{-1}$ at the surface, and 0.5 and $1 \times 10^{-5}$ K$^{-1}$ at the CMB. For models with $\alpha$ depth dependent, the constant $d$ was chosen between 1.7 and 2.2 which gives a value of $\alpha$ between 4.2 and $4.9 \times 10^{-5}$ K$^{-1}$ at the surface and between 0.5 and $0.8 \times 10^{-5}$ K$^{-1}$ at the CMB. The mean thermal Rayleigh number is then $5.8 \times 10^6$. However, at the surface, since the viscosity is one order of magnitude lower than in the lower mantle, $Ra = 5.8 \times 10^7$ for constant $\alpha$ and is around $10^8$ when $\alpha$ is depth dependent.

At the top and bottom surfaces we impose zero vertical velocity and horizontal free slip ($U_z = 0 = \partial U_x/\partial z$). The temperature is kept constant at the top surface ($\theta = 0$) and at the bottom ($\theta = 1$). Periodic boundary conditions for velocity and temperature are imposed at the sidewalls. Since we use $300 \times 100$ square elements the resolution is 29 km/element. In order to respect the volumetric proportions between the volume of the Earth's mantle ($V_{\mathrm{mantle}}$) and the volume of our domain in Cartesian geometry, we consider that each of the 30 000 elements of the grid represents a volume $V_{\mathrm{el}} = V_{\mathrm{mantle}}/30\,000$. As a consequence the viscosity jump at 670 km depth is modeled at 1000 km depth, in order to respect $V_{\mathrm{UM}} = V_{\mathrm{mantle}}/3$.

## 2.2. Modeling chemical heterogeneities with active tracers

We consider four possible distinct geochemical components: (i) the reference degassed mantle, (ii) the oceanic crust that upon subduction transforms into eclogite, (iii) the oceanic lithosphere, (iv) a reservoir chemically denser and less degassed than the reference mantle. These four components are modeled by using three families $f$ of tracers, thereafter denoted as: $f = 1$ for the oceanic crust, $f = 2$ for the denser, poorly degassed layer and $f = 3$ for the oceanic lithosphere. Each tracer belonging to a family $f$ represents a volumic fraction of an element $\chi_f$ thus a fraction of $V_{\mathrm{mantle}}$. The concentrations of six chemical species $i$ (i.e. $^{238}$U, $^{235}$U, $^{232}$Th, $^{40}$K, $^{4}$He, $^{3}$He) are attributed to the reference degassed mantle ($C_{\mathrm{DM}}^i$) and to each tracer of each family ($\Delta C_f^i$). The later are actually 'concentration anomalies' because they only represent differences with respect to the reference mantle and are meaningless alone.

### 2.2.1. Tracers initial concentration of U, Th, K, He

The mechanisms responsible for continental crust formation are still poorly understood, therefore to avoid modeling the formation of the continental crust, we start our model at $t_0 = 2$ Gyr before present, which corresponds to the mean age of the continental crust [27]. Thus we implicitly assume that all the continental crust was cre-

ated before $t_0$ and we neglect any possible influence on the geochemical processes. We also assume that the time scale of the processes responsible for the formation of the denser layer is relatively short with respect to the time scale of mantle convection. In other words, we implicitly consider that the denser layer formed rapidly before 2 Gyr BP. This hypothesis and its effect on the stability of the denser layer through time will be discussed later.

For each chemical species $i$, we need to assign the initial concentrations (i.e. at $t_0 = 2$ Gyr before present) $C_{\mathrm{DM}}^i$ to the degassed mantle and $\Delta C_f^i$ to each tracer of family $f$. This is done by using present-day concentrations of $^{4}$He and $^{238}$U and present-day isotopic ratios of $^{4}$He/$^{3}$He, Th/U, $^{235}$U/$^{238}$U and $^{40}$K/K for a mantle with two distinct reservoirs: a 'depleted' mantle and a 'primitive' mantle (see Table 1). The initial concentrations for the denser, relatively undegassed layer and for the overlying degassed mantle are calculated using the values given in Table 1, corresponding to 'primitive' mantle and to 'depleted' mantle, respectively. We calculate the initial concentrations back to $t = t_0$ solving for the radioactive decay of U, Th and K:

$$n_{i_{\mathrm{r}}}(t) = n_{i_{\mathrm{r}}}(t_0)\mathrm{e}^{-\lambda^{i_{\mathrm{r}}}t}, \tag{9}$$

and for the production of $^{4}$He by U and Th decay:

$$\frac{\mathrm{d}n_{^4\mathrm{He}}}{\mathrm{d}t} = 8\frac{\mathrm{d}n_{^{238}\mathrm{U}}}{\mathrm{d}t} + 7\frac{\mathrm{d}n_{^{235}\mathrm{U}}}{\mathrm{d}t} + 6\frac{\mathrm{d}n_{^{232}\mathrm{Th}}}{\mathrm{d}t}, \tag{10}$$

where $n$ is the number of mole of a chemical species and $\lambda^{i_{\mathrm{r}}}$ is the decay constant of the radioac-

Table 1
Present-day ratios and concentrations

|  | 'Depleted' | 'Primitive' |
|---|---|---|
| $^{4}$He/$^{3}$He [43] | 88 000 | 25 000 |
| $^{4}$He (cm$^3$ STP/g)[a] | $10^{-5}$ | $10^{-4}$ |
| $^{238}$U (ppb) [44] | 6 | 22 |
| Th/U [19] | 2.7 | 4.2 |
| K/U [19] | 12 700 | 12 700 |
| $^{235}$U/$^{238}$U | 1/137.88 | 1/137.88 |
| $^{40}$K/K | $1.19 \times 10^{-4}$ | $1.19 \times 10^{-4}$ |
| Mass (g) | $1.33 \times 10^{27}$ | $2.66 \times 10^{27}$ |
| Volume | $(1/3)V_{\mathrm{mantle}}$ | $(2/3)V_{\mathrm{mantle}}$ |

[a] Moreira, personal communication, 2001.

Table 2
Calculated initial concentrations at $t = 2$ Gyr BP

| Element | Degassed mantle | Undegassed layer |
|---|---|---|
| $^{238}$U (ppb) | 3.61 | 79.43 |
| $^{235}$U (ppb) | 0.134 | 3.05 |
| $^{232}$Th (ppb) | 7.95 | 272.03 |
| $^{40}$K (ppb) | 12.21 | 268.66 |
| $^{3}$He (cm$^3$ STP/g) | 6.73 $10^{-11}$ | 6.32 $10^{-9}$ |
| $^{4}$He (cm$^3$ STP/g) | $3.21 \times 10^{-6}$ | $8.60 \times 10^{-5}$ |
| Volume | $(3/4)V_{mantle}$ | $(1/4)V_{mantle}$ |

tive element $i_r$. Following [28] the used values are: $\lambda^{238}U = 1.55125$, $\lambda^{235}U = 9.8485$, $\lambda^{232}Th = 0.4948$, $\lambda^{40}K = 5.543$ ($\times 10^{-10}$ yr$^{-1}$). We remark that all the calculations respect mass balances and that the calculated initial $^3$He concentration is of the same order as the post-accretion lower bound $^3$He inferred from chondrites [29]. The initial concentrations for the relatively undegassed layer are

given in Table 2 under 'undegassed layer', while the surrounding mantle has the initial concentrations given in Table 2 under 'degassed mantle'. In most of our models the initial volume of the denser layer is 25% of the whole mantle volume.

The temperature field for the initial condition (Fig. 1a) is obtained by running the convection code until steady state without tracers and with homogeneous concentrations in heat producing elements, corresponding to the mean concentration of U, Th and K at $t_0 = 2$ Gyr BP. At time $t = t_0$ we insert 25 active tracers per element to represent the chemically denser layer and start the thermochemical convection simulation.

### 2.2.2. Tracers advection and time evolution of the concentrations

Tracers advection at each time step is performed using a bicubic spline interpolation within the mesh of the model [30] and a second-order
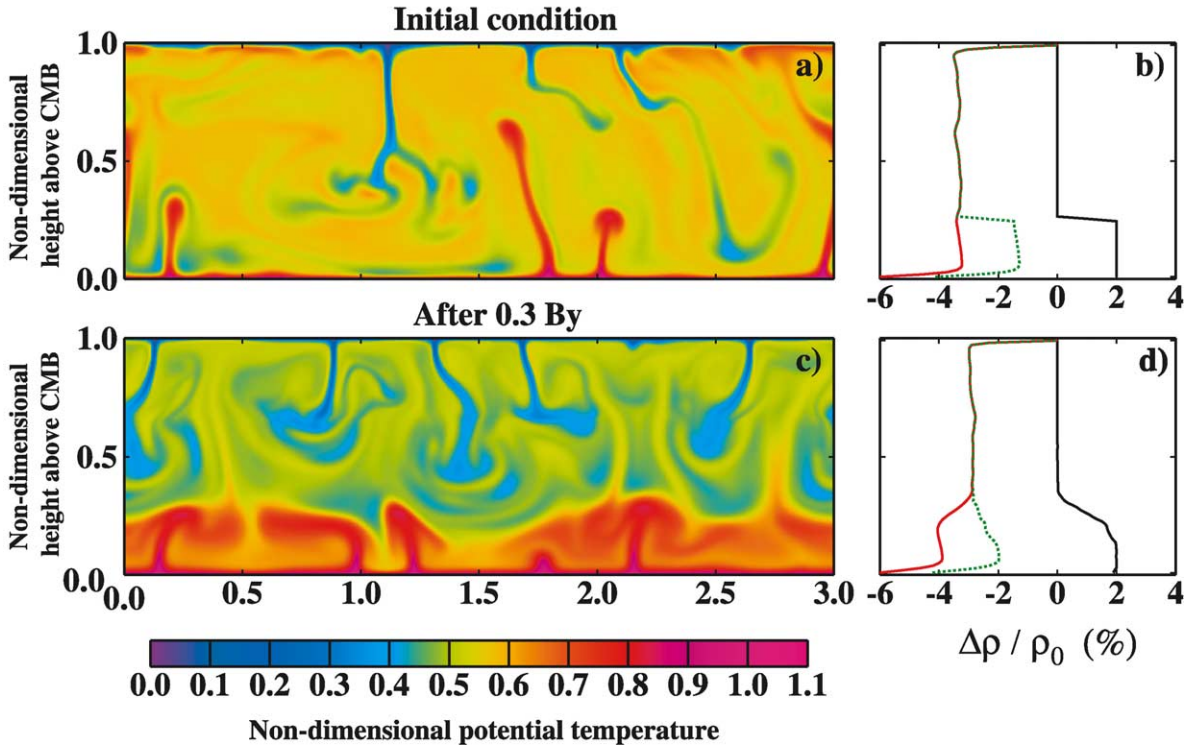


Fig. 1. Model 1: Temperature field (left). Horizontally averaged density profiles (right): $\Delta\rho_{chemical}/\rho_0$ (black), $\Delta\rho_{thermal}/\rho_0$ (red), $\Delta\rho_{effective}/\rho_0$ (green dashed line). Initial condition (top). After elapsed time 0.3 Gyr (bottom).

Runge–Kutta method for the time scheme. The advection of active tracers reproduces well the thermochemical benchmark [24], as shown in Appendix B.

Due to the radioactive decay, the concentration of each radiogenic species $i_r$ and of $^4$He for each tracer is a function of time according to Eqs. 9 and 10 which can be rewritten as follows:

$$\Delta C_f^{i_r}(t) = \Delta C_f^{i_r}(t_0)e^{-\lambda^{i_r} t} \tag{11}$$

$$\Delta C_f^{^4\text{He}}(t) = 4\left[\frac{8}{238}\Delta C_f^{^{238}\text{U}}(t)(e^{\lambda^{^{238}\text{U}}t}-1)\right.$$
$$+ \frac{7}{235}\Delta C_f^{^{235}\text{U}}(t)(e^{\lambda^{^{235}\text{U}}t}-1)$$
$$\left.+ \frac{6}{232}\Delta C_f^{^{232}\text{Th}}(t)(e^{\lambda^{^{232}\text{Th}}t}-1)\right]. \tag{12}$$

At each time step, and for each element *el* of the mesh, the code also calculates the volumic fraction represented by the tracers present in each element:

$$\chi_{\text{el}} = \sum_{f=1}^{3}\chi_f \tag{13}$$

We calculate the concentration of each chemical species $i$ in each element *el* using:

$$C_{\text{el}}^i = C_{\text{DM}}^i + \sum_{f=1}^{3}\Delta C_f^i \chi_f, \tag{14}$$

where $C_{\text{DM}}^i$ represents the concentration of a species $i$ for the depleted mantle without heterogeneities. This equation (which is, in its form, similar to Eq. 6) illustrates well the principle on which our modeling of chemical heterogeneities is based, since it shows that tracers represent only the chemical differences with respect to the reference degassed mantle. For instance, if there are no tracers in an element, $\chi_{\text{el}}$ will be 0 and $C_{\text{el}}^i$ will be equal to $C_{\text{DM}}^i$. Note that also $C_{\text{DM}}^i$ varies with time according to Eqs. 11 and 12.

The chemical density anomaly for each element $\Delta \rho_c^{\text{el}}$ is:

$$\Delta \rho_c^{\text{el}} = \rho_0 \sum_{f=1}^{3}\beta_f \chi_f \tag{15}$$

For the crust $\beta_1 = 0.02$, since we assume that the subducted crust becomes 2% denser than the surrounding mantle [31]. For the chemically dens-

er layer $\beta_2 = \Delta\rho_c/\rho_0$, the chemical density excess $\Delta\rho_c$ is a parameter that we vary systematically, as discussed later. Since the subducted lithosphere remains neutrally buoyant $\beta_3 = 0$.

The non-dimensional internal heating for each element is: $H_{\text{el}}^{i_r} = H^{i_r}C_{\text{el}}^{i_r}$. Following [28] the heat production rates $H^{i_r}$ are: $H^{^{238}\text{U}} = 9.37$, $H^{^{235}\text{U}} = 56.9$, $H^{^{232}\text{Th}} = 2.69$, $H^{^{40}\text{K}} = 2.79$ ($\times 10^{-5}$ W kg$^{-1}$).

## 2.3. Modeling ridges and hotspots

The location of divergent and convergent zones is not imposed as a boundary condition, but is entirely governed by mantle motion. Therefore, at each time step the code has to detect the location of 'ridges' and 'hotspots'. Although the model is two-dimensional, it is possible to make a distinction between ridges and hotspots based on the following statements. We define a ridge where the surface flow is divergent due to the presence of convergent zones on both sides of it. At this location the number of 'crust tracers' decreases in the top row of elements. We locate a ridge wherever the number of 'crust tracers' that have never been subducted becomes equal to zero. At a ridge, we simulate the formation of a 7.25 km thick (1/4 of an element mesh) oceanic crust by adding crustal tracers in the upper part of the top element, while the formation of a 79.75 km thick depleted oceanic lithosphere is modeled by adding lithospheric tracers. We calculate the concentrations in the residual solid and in the melt assuming equilibrium melting:

$$C_{\text{solid}}^i = \frac{C_0^i}{D_{\text{sol}\to\text{melt}}^i + F(1-D_{\text{sol}\to\text{melt}}^i)}, \tag{16}$$

$$C_{\text{melt}}^i = \frac{C_{\text{solid}}^i}{D_{\text{sol}\to\text{melt}}^i}, \tag{17}$$

where $D_{\text{sol}\to\text{melt}}^i$ is the solid–melt partition coefficient of a chemical species $i$. For U, Th and K, $D_{\text{sol}\to\text{melt}}^i = 0.01$ [32]. For $^4$He and $^3$He $D_{\text{sol}\to\text{melt}}^i = 0.001$.

Moreover, to simulate degassing processes the calculated $C_{\text{melt}}^{\text{He}}$ is divided by $10^5$. $C_0^i$ is the concentration of the solid before partial melting and it corresponds to the mean concentration of the species $i$ in the top three elements of the model

where we assume that partial melting occurs. In order to be consistent with mass balances, the melt fraction $F$ corresponds to the ratio of crustal thickness $h_{crust}$ over the total thickness $h_{lithosphere} + h_{crust}$. $F$ is thus assumed constant and equal to 8.3%. The concentrations $\Delta C_f^i$ for each added tracer are then calculated using Eq. 14, considering that $C_{el}^i = C_{melt}^i$ for the newly formed crust and that $C_{el}^i = C_{solid}^i$ for the residual lithosphere.

At each time step the code also has to detect the location of rising plumes according to the following criteria: (1) plume material should be at least 30% hotter than the average temperature of the degassed mantle [33], (2) the tracers should come from a depth greater than $z_{plume} = D/2$, since the thermal boundary layer where plumes originate is located below $z_{plume}$. This way of detecting plumes and ridges also allows us to detect a plume under a ridge. For plumes the zone of partial melting extends from 87 to 116 km depth and the melt fraction is $F = 8.3\%$.

In order to respect mass balance, the volumic fraction $(\chi_f)$ associated to a tracer of a family $f$ may change, as a consequence of partial melting in a plume. Therefore, if the volumic fraction represented by a tracer in a plume before melting is $\chi_f$, the volumic fraction associated to the added tracer will be $\chi_f^{melt} = F\chi_f$ (which will be added in the first top row element, between 0 and 7.25 km depth) and for the residual solid tracer $\chi_f^{solid} = (1-F)\chi_f$ (located at the position of the 'plume' tracer before melting). The mass balance is therefore satisfied: $\chi_f^{melt} C_{melt} + \chi_f^{solid} C_{solid} = \chi_f C_0$. Note that mass conservation for the chemical species (except for helium which is degassing) is satisfied at each time step. In other words, if there was no radioactive decay and no degassing, the total mass of U, Th, K and He would be constant with time. This guarantees the self-consistency of the method used to describe chemical heterogeneities and melting zones. Other technical aspects of the modeling and a benchmark are given in Appendices A and B.

## 2.4. Dimensionless parameters

Four dimensionless parameters are varied systematically:

Table 3
Models and destabilization time $\tau$ of the denser layer

| Model | $B$ | $\eta$ | $\alpha$ | $d$ | $H$ | $\zeta$ | $\tau$ (Gyr) |
|---|---|---|---|---|---|---|---|
| 1 | 0.33 | cst. | cst. | – | yes | 0.25 | 0.6 |
| 2 | 0.33 | cst. | cst. | – | yes | 0.12 | 0.4 |
| 3 | 0.33 | cst. | cst. | – | no | 0.12 | 0.5 |
| 4 | 0.33 | cst. | $\alpha(z)$ | 1.7 | yes | 0.25 | 0.9 |
| 5 | 0.33 | $\eta(T)$ | $\alpha(z)$ | 1.7 | yes | 0.25 | 1.2 |
| 6 | 0.33 | cst. | $\alpha(z)$ | 1.7 | no | 0.25 | 1.4 |
| 7 | 0.66 | cst. | $\alpha(z)$ | 1.7 | yes | 0.25 | > 7.8 |
| 8 | 0.42 | $\eta(T)$ | $\alpha(z)$ | 2.2 | yes | 0.25 | > 2.3 |
| 9[a] | 0.83 | cst. | cst. | – | yes | 0.25 | > 2.2 |

[a] Initial temperature condition different from Models 1–8.

(1) The buoyancy number $B$ may be varied in two ways: (i) By changing the chemical density excess $\Delta\rho_c$ of the relatively undegassed layer with respect to the overlying mantle. Here we explore a range of $\Delta\rho_c/\rho_0$ between 1 and 4%. (ii) By changing the depth dependence of the thermal expansion coefficient, since this modifies the effective buoyancy of the hot deep material. We investigate a plausible range of values for the constant $d$ from 1.7 to 2.2.

(2) The viscosity ratio between the two layers is equal to 1 for models with constant viscosity, while for models with temperature dependent viscosity, the thermal evolution of the system leads to a viscosity contrast between the hot deep layer, enriched in radiogenic elements, and the overlying colder mantle. Therefore, the lower layer becomes less viscous than the overlying mantle, thus leading to a temperature-induced viscosity contrast between the two layers.

(3) The non-dimensional internal heating $H_r$ depends on the radiogenic element concentrations. We have run only two models without internal heating to assess the effect of radiogenic heat on the stability of the denser layer.

(4) The thickness ratio $\zeta = h_{layer}/D$. For most models the initial volume of the denser layer corresponds to 25% of the whole mantle volume ($\zeta = 0.25$), but we also consider a smaller initial volume ($\zeta = 0.12$). Table 3 shows our choice of parameters for the models described in detail in the following section.

## 3. Results

In the first part, we investigate the stability of the denser layer and explore the role of several physical parameters in inhibiting mixing and convective destabilization of the layer. In the second part, we study a model for which the denser layer remains stable and geochemically distinct for more than 2 Gyr after $t_0$. In order to compare our model predictions with geochemical observations we calculate $^3He/^4He$ ratios that mark the difference between MORB and OIB.

### 3.1. Stability of the denser layer

Fig. 1a shows the initial temperature field used for all simulations (except for Model 9), the corresponding average density profile is shown in Fig. 1b. At this time we introduce the active tracers and the vertical profile for $\Delta\rho_c/\rho_0$ shows the sharp jump marking the top of the chemical layer. Fig. 1c shows the temperature field after 0.3 Gyr for Model 1 with constant $\alpha$ and constant stratified viscosity. The chemically denser material has a profound effect on the dynamics: the two layers convect separately and a thermal boundary develops at their interface. The bottom layer, enriched in radiogenic elements heats up, while the overlying mantle cools, due to the inefficient conductive heat transfer across the layers. Therefore, in the bottom layer the positive thermal buoyancy increases and competes with the negative buoyancy of chemical origin (Fig. 1d). Convective destabilization occurs after the time $\tau = 0.5$ Gyr from the initial condition.

Model 2 is the same as Model 1 except for a reduced thickness ratio $\zeta = 0.12$. Decreasing the initial thickness of the denser layer causes a faster destabilization ($\tau = 0.4$ Gyr). Note that in order to be consistent with mass balances, the volume reduction of the denser layer leads to higher initial concentration of the heat producing elements in the layer, and thus to a higher internal heat production. However, a thin layer ($\zeta = 0.12$) would rapidly destabilize ($\tau = 0.5$ Gyr) even without internal heat (Model 3). In other models (not shown here) we also find that for constant thermal expansion coefficient a relatively thin layer remains

stable only if the chemical density excess is at least 4%.

For Model 4 all the physical parameters are as in Model 1, except for the depth dependent thermal expansion coefficient. In agreement with Hansen and Yuen [34] we find that the stability of the denser layer is enhanced by a decrease of $\alpha$ with depth (see Table 3).

Model 5 differs from Model 4 by having temperature dependent viscosity, which has a stabilizing effect. The large viscosity contrast across the two convecting layers helps to prevent global convection and mass exchange between the hot, less viscous basal layer and the overlying more viscous mantle, even if the effective density contrast between the two layers is equal to zero. The calculated destabilization time is $\tau = 1.2$ Gyr, after which the system evolves into whole mantle convection.

Model 6 is directly comparable to Model 4, except for being entirely bottom heated. We include the denser layer ($B = 0.33$) but do not consider the radiogenic heat production. Also in this case the destabilization time is increased ($\tau = 1.4$ Gyr), showing that internal heat production accelerates the destabilization of the denser layer.

We find that for a given chemical density excess, the physical parameters inhibiting destabilization and mixing of the denser layer are a thermal expansion coefficient decreasing with depth, a temperature dependent viscosity and a lower in-
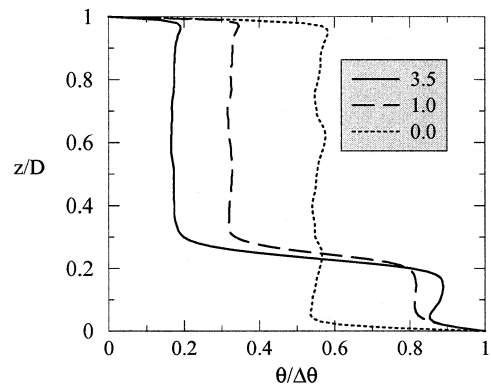


Fig. 2. Model 7: Non-dimensional temperature vs. non-dimensional height of the model domain. Horizontally averaged temperature profiles at the initial time, after 1 Gyr and after 3.5 Gyr.
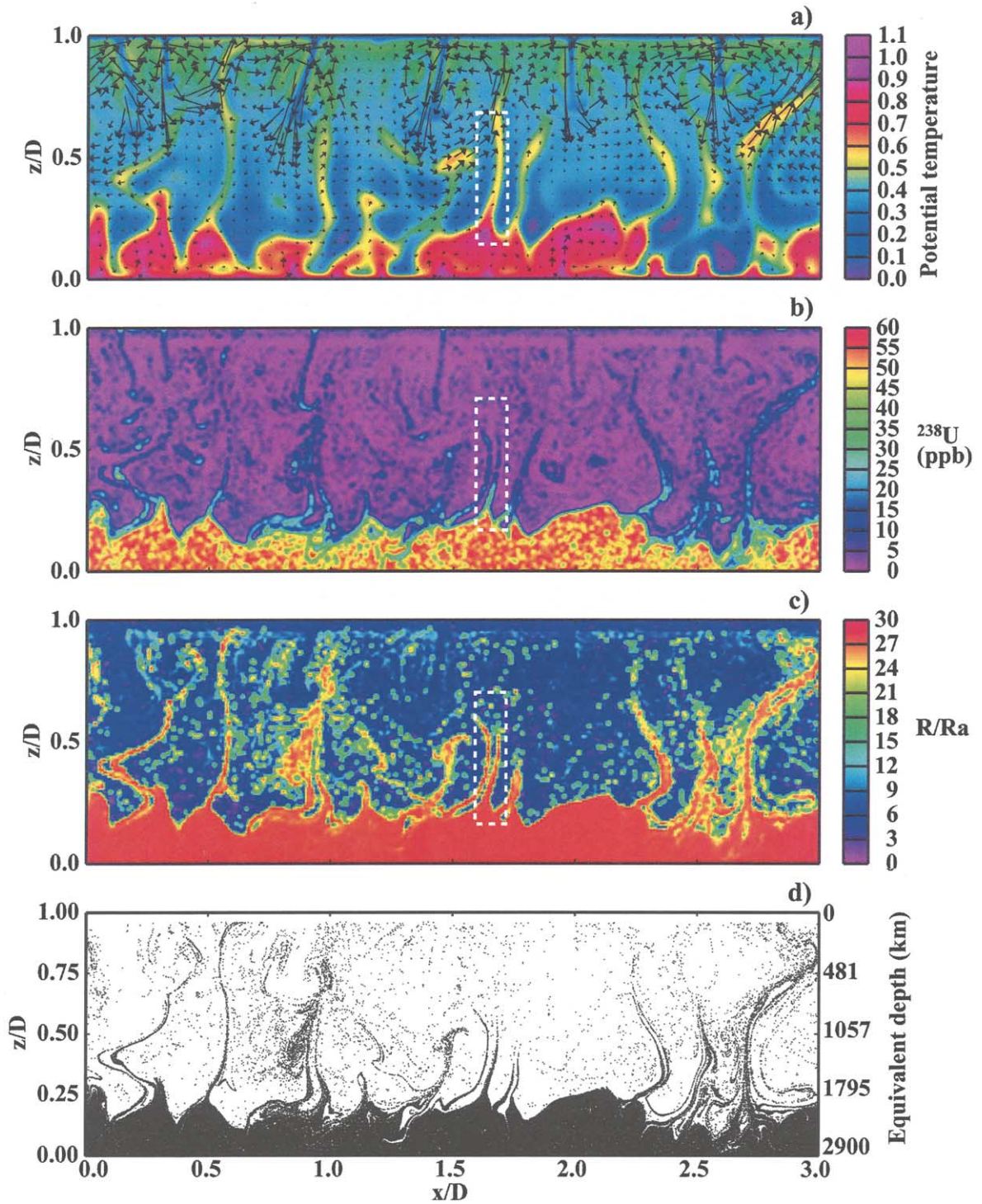
Fig. 3. Model 8 after the elapsed time $t_e = 2.1$ Gyr: (a) Temperature and velocity fields, (b) $^{238}$U, (c) R/Ra, (d) tracers for the denser and relatively undegassed material. The rectangle delimits the area shown in detail in Fig. 5d.

ternal heat production. Moreover, for relatively low density contrast, the layer does not remain stable for more than 2 Gyr.

In Model 7 we consider a stronger chemical density excess ($B = 0.66$), with all the other parameters as in Model 4. The layer remains stable for more than 7 Gyr and the interface does not develop any topography. The temperature profiles at different times (Fig. 2) show that a sharp thermal boundary forms between the two convective layers. However, this model is unrealistic, since there is no geophysical evidence for such a sharp interface in the lower mantle.

### 3.2. Model with a stable layer for more than 2 Gyr after $t_0$

Model 8 has temperature dependent viscosity, a stronger decrease of $\alpha$ with depth, compared with the previous cases, and an intermediate chemical

density excess $\Delta\rho_c/\rho_0 = 2.4\%$ (i.e. $\Delta\rho_c = 100$ kg/m$^3$ and $B = 0.42$). The denser layer remains stable and geochemically distinct for more than 2.3 Gyr. Note that since we assume the Boussinesq approximation, the chemical density excess given above is equivalent to a $\Delta\rho_c/\rho_0$ at ambient pressure and temperature in a compressible case. Fig. 3a shows the temperature field at elapsed time $t_e = 2.1$ Gyr after $t_0$. Note that, since $t_0$ is 2 Gyr BP, an elapsed time $t_e = 2.1$ would represent present-day time. The denser layer at the bottom has a variable thickness and forms 'domes' that scaled to the Earth would extend from the CMB to 1800 km depth. Slabs may sink to the CMB, or may accumulate on top of the layer, while plumes originate from the thermal boundary at the interface between the denser layer and the overlying mantle. At $t_e$, the average surface heat flux is 72 mW/m$^2$ while the estimated crust subduction rate ranges between 10 and 30 km$^3$/yr, which is of the
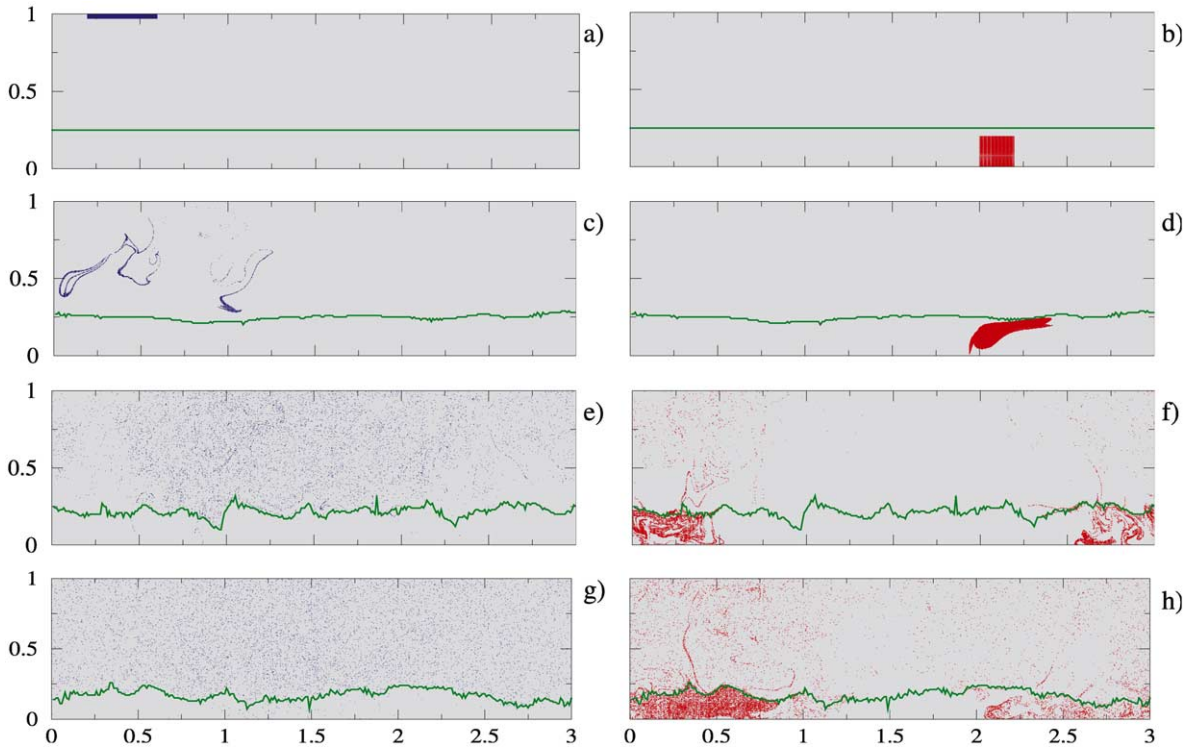


Fig. 4. Model 8: Evolution of the position of two families of passive tracers at elapsed time $t_e = t_0$ (a, b), $t_e = 0.1$ Gyr (c, d), $t_e = 1$ Gyr (e, f) and $t_e = 2.1$ Gyr (g, h). The green curve shows the interface between the denser layer and the overlying mantle.

same order as the 20 km$^3$/yr estimated for the Earth [28]. The rms surface velocity at $t_e$ is 1 cm/yr.

### 3.2.1. Stirring and mass exchange between the two layers

To estimate the stirring efficiency within each layer, we advect 'blocks' of passive tracers (in addition to the active tracers). We use one 'block' (87 km thick and 1160 km long) initially in the uppermost mantle (Fig. 4a), and a square 'block' of 580 km size initially in the denser layer (Fig. 4b).

After 0.1 Gyr it is evident that stretching, folding and transport in the upper layer (Fig. 4c) are more efficient than in the denser layer (Fig. 4d) mainly due to Rayleigh number, an indicator of the vigor of convection, which is higher in the upper layer than in the denser layer. After 1.1 Gyr tracers initially in the upper mantle are dispersed all over the upper layer (Fig. 4e) and a very small fraction (ca. 2%) has penetrated in the denser layer. On the contrary, tracers initially in the denser layer are weakly dispersed by convection (Fig. 4f) and a small fraction (ca. 12%) has been brought in the upper layer by thermal plumes. After the elapsed time $t_e = 2.1$ Gyr tracers are uniformly distributed all over the upper degassed layer, indicating efficient stirring (Fig. 4g), while in the denser and relatively undegassed layer homogenization is weak (Fig. 4h) and regions with virtually no tracers coexist with zones at high tracers concentration. Roughly 3% of the tracers initially in the upper mantle are incorporated in the denser layer, while less than 25% of tracers has escaped from the denser layer.

Therefore, the two layers have a different dynamics: the upper layer convects vigorously and stirring is efficient, while in the denser layer convection is sluggish and stirring is inhibited. For a more rigorous study of mantle stirring in thermochemical convection see [35].

### 3.2.2. Helium ratios at ridges and hotspots

Stirring and mass exchange between the different reservoirs have a direct influence on helium ratios and on the concentration of radioelements at ridges and hotspots. Fig. 3b shows the concen-

tration of $^{238}$U after the elapsed time $t_e = 2.1$ Gyr for Model 8. We note that since U, Th, and K have the same partition coefficients, their space distribution will be as in Fig. 3b, obviously their concentrations will be different, depending on the decay constant and on the initial concentration of each element. The concentration of $^{238}$U is quite homogeneous in each reservoir. In the overlying and depleted mantle, the concentrations are lower than 10 ppb, except within the crustal part of sinking slabs, enriched in incompatible elements, and within plumes. These heterogeneous concentrations tend to be quickly homogenized by efficient stirring. In the denser and relatively undegassed layer, $^{238}$U concentrations are around 55 ppb, due to the high initial concentration and to the limited entrainment of overlying 'depleted' material.

The calculated R/Ra ratio (Fig. 3c) is around 30 within the denser layer and around 8–10 in the overlying mantle, where R/Ra can locally be as low as 0–3 or as high as 25–28. Low R/Ra ratios are due to the presence of old recycled oceanic crust. Recycled material is enriched in $^4$He producing elements (i.e. U and Th) and has low He concentrations because of degassing, therefore its $^3$He/$^4$He decreases rapidly with time. High R/Ra ratios are due to the presence of plumes which carry a fraction of relatively undegassed deep material with high $^3$He/$^4$He and high helium concentrations. Fig. 3d shows the position of the tracers representing the relatively undegassed layer. More than 75% of the tracers initially present in the layer are still trapped in the 'undegassed material', while the remaining have been entrained by plumes.

For the last 150 Myr before the time $t_e = 2.1$ Gyr, we calculate the R/Ra ratios for MORB and for OIB. During this period all the melting zones for hotspots and ridges are considered as plume and ridge 'samples', respectively. Over the last 150 Myr before $t_e = 2.1$ Gyr, we have 16 947 plume samples and 499 ridge samples. For MORB (Fig. 5a) the narrow spectrum of R/Ra values, centered around 7–8, reflects the efficient stirring in the upper part of the mantle. For OIB (Fig. 5b), the spectrum of R/Ra values is much larger, ranging from 0 to 28. Note that the 'gap'
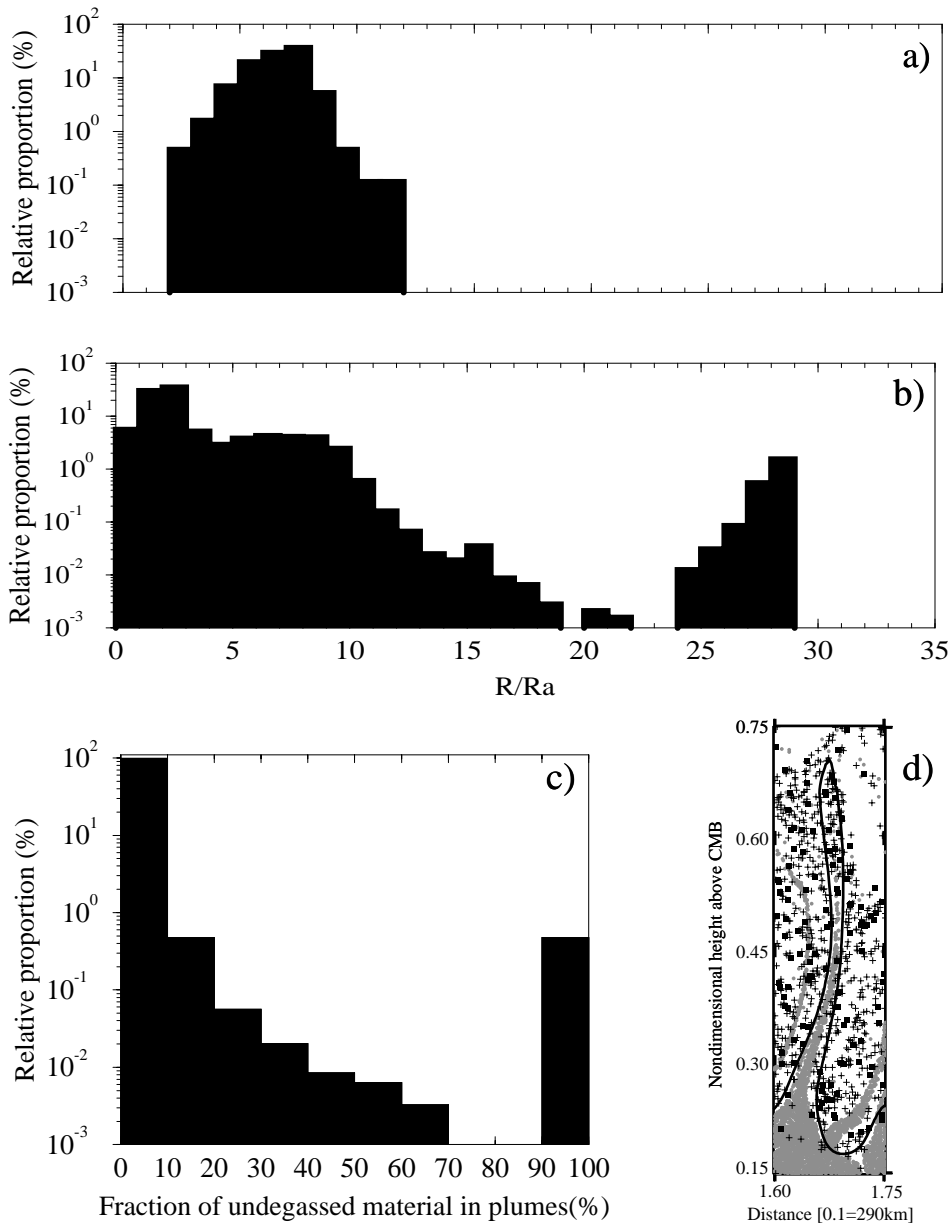
Fig. 5. Model 8: MORB and OIB formed in the last 150 Myr before $t_e$. (a) R/Ra for MORB (499 'samples'), the proportion is relative to the total volume of MORB created in the considered time span. (b) R/Ra for OIB (16 947 'samples'), the proportion is relative to the total volume of OIB created in the considered time span. (c) Fraction of relatively undegassed material present in plumes, relative to the total volume of plumes. (d) Detail of the plume shown in Fig. 3c. The solid line delimits the plume, following the excess temperature criterion. For sake of clearness we show only tracers coming from a depth greater than $z = 0.5$. Tracers symbols: for the denser and relatively undegassed material (gray circles), subducted oceanic crust (squares), subducted lithosphere (crosses).

(around R/Ra = 19–24) observed in R/Ra ratios is probably an artifact due to random fluctuations of the number of tracers in plume samples (see Appendix D). Roughly 3% of our plume samples have R/Ra between 26 and 28, while nearly 65% of our plume samples have R/Ra lower than average MORB material. Such low ratios are due to old recycled oceanic crust, which contains high $^4$He resulting from the decay of U and Th. The remaining 32% of our plume samples have intermediate R/Ra, due to mixing between recycled oceanic crust/lithosphere and relatively undegassed material. Note that helium ratio depends (i) on the time interval during which the material was isolated, (ii) on the initial concentration of $^4$He and $^3$He, (iii) on the concentrations of $^4$He producing elements. Therefore, R/Ra values are not directly proportional to the R/Ra values of the different sources but rather to the concentrations of $^3$He and $^4$He.

Fig. 5c shows the fraction of relatively undegassed material present in mantle plumes for the same time interval. We find that 0.5% of all the plume samples contains more than 90% of relatively undegassed material coming from the denser layer, another 0.5% contains recycled oceanic crust and lithosphere mixed with 10–20% of relatively undegassed material, while the remaining 99% of the plume samples contains more than 90% of recycled oceanic crust or lithosphere.

A great range of compositions may provide the same R/Ra ratio. For example, if we consider plumes with R/Ra = 26 we find that tracers coming from the denser layer represent on average 8% (with a maximum of 19% and a minimum of 4%), tracers for the oceanic crust represent on average 8% (with a maximum of 17%) and tracers for the lithosphere represent on average 83%. The heterogeneous nature of plumes is also illustrated in Fig. 5d where we show all the tracers incorporated in a plume. Relatively undegassed and enriched material coming from the denser layer, as well as recycled oceanic crust and lithosphere are entrained in the plume.

Different degrees of mixing between the three sources considered here (i.e. recycled oceanic crust, recycled lithosphere and relatively undegassed material) generate the large spectrum of

R/Ra values for OIB, in agreement with recent He–Ne geochemical studies [17].

## 4. Discussion

Our results on the stability of the denser layer are obtained with a two-dimensional model and we should discuss to which extent 2D results can be extrapolated to the three-dimensional spherical Earth. It is clear that adding a third degree of freedom influences the efficiency of mixing, especially when viscosity is temperature dependent. In such case toroidal motions, which enhance mixing [36], add to the poloidal motions present in 2D or in 3D with constant viscosity [37]. At present the toroidal motions account for only one third of the total [38], they decrease rapidly with depth and may not exist at the bottom of the mantle [39]. Three-dimensional laboratory experiments of thermochemical convection [5] show that a denser layer with $B$ less than 0.17 can remain stable for ages comparable to the age of the Earth. We should notice that these analog experiments do not include internal heating and have rigid boundary conditions. Therefore, it seems difficult to predict the $\Delta\rho_c$ necessary to keep unmixed a chemically denser and primitive layer, by extrapolating our 2D results. Independent of the geometry, however, the presence of a stable, poorly degassed and denser material will produce (1) a large spectrum of He ratios for OIB, because of the different sources incorporated by ascending plumes and (2) a sharp spectrum of R/Ra ratios for MORB, because of the efficiency of stirring in the overlying mantle, probably further enhanced by the surface toroidal motions.

We are aware that the appropriate Rayleigh number for the Earth's mantle is higher than the value we used. Montague and Kellogg [40] showed that mixing of a denser basal layer a few hundred kilometers thick is less efficient at higher Rayleigh numbers. Therefore, the critical value of the buoyancy number $B$ needed to produce stable layering decreases as the Rayleigh number increases.

In most of our models we have chosen a volume of the denser layer equal to one fourth of the

whole mantle volume but this was a rough estimate based on tomographic studies [8] that suffer from the lack of resolution at greater depths. This parameter is therefore poorly constrained and the existence of a 1000 km thick denser layer in the lower mantle is controversial among seismologists. However, one can expect that even a thicker denser layer that remains stable until present-day time will produce the same effect on helium ratio for MORB and OIB. This does not necessarily imply a chemical density contrast much higher than 2.4% for the denser layer since we have assumed no viscous heating for all our models. This means a dissipation number $Di = (\alpha_0 g D)/C_p$ equal to zero, whereas a typical value for the Earth mantle would be 0.3–0.4. Numerical studies have shown that a realistic $Di$ greatly increases the stability of the denser layer in thermochemical convection [41]. Our initial condition implies that the time scale for the formation of the denser layer is short with respect to mantle convection time scale. Since there is no certainty about the processes responsible for the existence of such denser and poorly degassed material in the mantle, it seems difficult to speculate about the age and time scale of its formation. As said before, we decided to start 2 Gyr BP in order to avoid modeling the formation of the continental crust, which remains challenging. If we had started our models before 2 Gyr BP, the chemical density excess required to keep the layer stable should have been probably higher, due to the destabilizing effect of a higher internal heat production. The results of Model 7, where the layer remains stable for more than 7.8 Gyr, let us suppose that a $\Delta\rho_c/\rho_0$ of 4% is an upper bound for keeping the denser layer stable, even starting our models before 2 Gyr BP.

Finally, it is important to note that as long as the denser and less degassed layer remains stable or marginally stable until present-day, our helium results are insensitive to the initial temperature condition, as shown in Appendix C.

## 5. Conclusion

Chemically denser material at the base of the Earth's mantle profoundly affects the convection regime and the evolution of geochemical heterogeneities. We found that a layer with an initial volume equal to 25% of the whole mantle can remain geochemically distinct for more than 2.3 Gyr, even with a relatively small chemical density excess $\Delta\rho_c/\rho_0 = 2.4\%$ and a buoyancy ratio $B = 0.42$. By using active tracers we model the evolution (i) of the subducted oceanic crust and lithosphere, (ii) of the relatively primordial layer, which is enriched in radiogenic elements and in $^3He$, with respect to the overlying mantle. After 2.1 Gyr the denser material has developed a complex topography, with 'domes' extending up to 1000 km above the CMB. Plumes originate from the thermal boundary layer at the interface between the hot basal layer and the overlying colder mantle, while slabs may accumulate on top of the denser material, or may deflect it and sink to the CMB.

Tracers carry the concentrations of U, Th, K and He, allowing us to calculate the helium ratios for partial melts formed at spreading ridges and at hotspots. For ridges, the R/Ra shows a narrow spectrum, centered around 8, indicating that the source region is fairly homogeneous, well mixed and degassed. For plumes, the R/Ra shows a large spectrum from 0 up to 28, as a result of the heterogeneous nature of plumes. Three distinct geochemical components enter in variable proportions in our plumes: (i) ancient recycled oceanic crust, which induces very low and intermediate $^3He/^4He$ ratios, (ii) depleted oceanic lithosphere, which induces intermediate $^3He/^4He$ ratios, (iii) denser and relatively undegassed material, which induces high $^3He/^4He$ ratios. Although Sr–Nd–Pb isotopic variability in mantle plumes can be explained only by the presence of recycled material [9,13], noble gases observed in plumes indicate the presence of a relatively undegassed reservoir in the Earth's mantle [17,42].

The origin of a denser and poorly degassed layer still has to be investigated, however, we believe that our results capture a fundamental aspect of the geochemical differences between MORB and OIB, and that thermochemical convection may reconcile geochemical and tomographic observations.

## Acknowledgements

## Appendix A. Tracers' treatment

To properly describe heterogeneities, it is necessary to have enough tracers in each element of the mesh. If the number of tracers per element is too small, spurious effects like $\chi_{el} > 1$ may arise [13]. This implies for instance that the density anomaly induced by the presence of tracers could be greater than the maximum density anomaly $\Delta\rho_c$ initially set. Having enough tracers per element helps to minimize such effect but statistically it will never be completely canceled. For this reason if in some elements (except melting zones), the volume represented by the tracers is too important ($\chi_{el} > 1$), a correction weighted by $\chi_f$ will be applied in order to have $\chi_{el} = 1$. This correction has
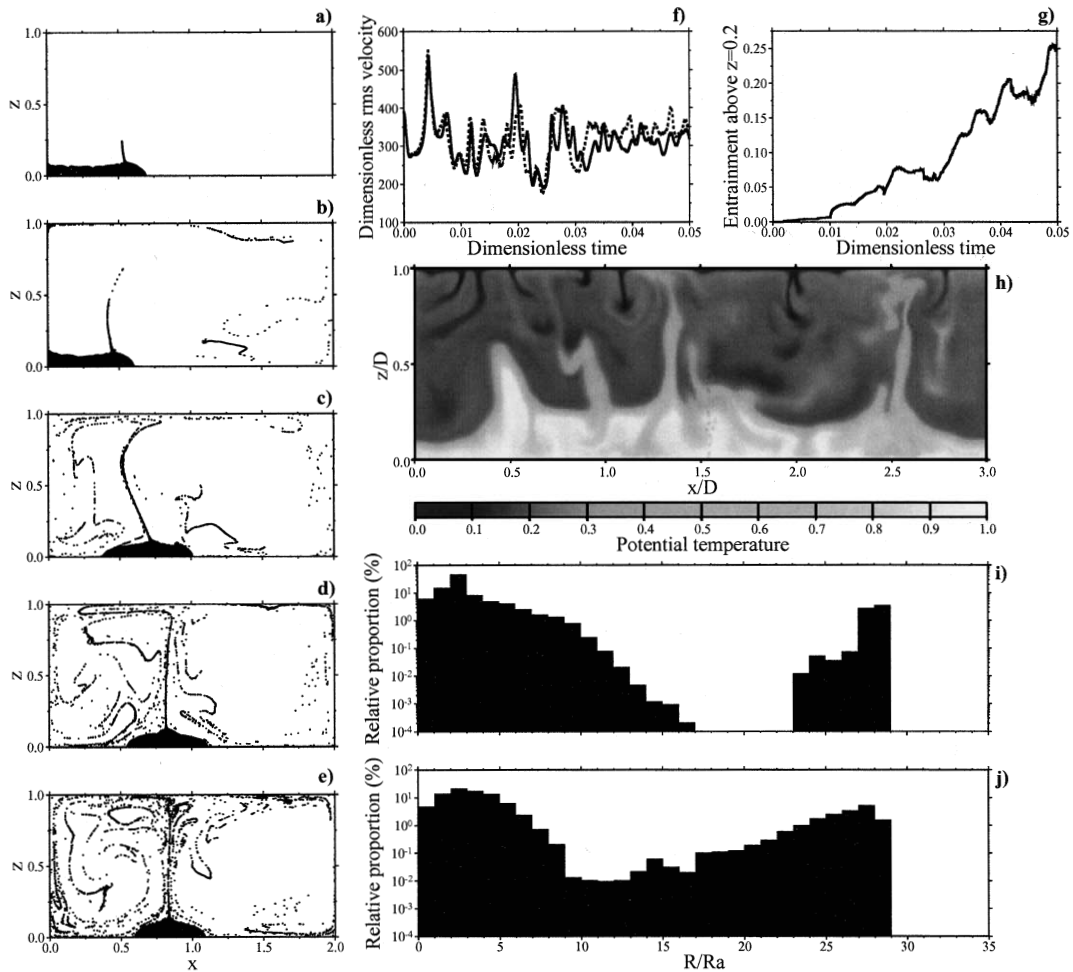


Fig. 6. (a–e) Snapshots showing the evolution of tracers positions. (f) rms velocity vs. dimensionless time. Solid line: no correction is applied. Dotted line: a correction is applied in zones where there are too many tracers. (g) Time evolution of entrainment. Model 9: (h) temperature field at elapsed time $t_e = 2.1$ Gyr, (i) R/Ra values for OIB (35 195 'samples') formed in the last 150 Myr before $t_e$. (j) Model 10: R/Ra values for OIB (45 529 'samples'), formed in the last 150 Myr before $t_e = 2.1$ Gyr.

been tested (see Appendix B). For melting zones, tracers are prevented to enter in the melting zone where $\chi_{el} = 1$, thus allowing us to respect mass conservation. We checked that there was no particular build up of tracers by comparing $\chi_{el}$ in the row element just below the zones where tracers are eventually prevented to enter with $\chi_{el}$ (before applying the corrections explained above) for the rest of the computational domain. No significant differences were found. Finally, in order to reduce the artificial overestimate of plume volcanism in our 2D Cartesian model, recycled hotspot material is not taken into account in future melting zones.

## Appendix B. Numerical benchmark

The implementation of active tracers and their advection was tested with a thermochemical benchmark [24]. We use a grid with $100 \times 200$ square elements and 25 tracers per element to model the density anomalies in the denser layer. Fig. 6a–g show the results that should be compared with those in [24]. Our implementation of active tracers and their advection reproduces well the thermochemical benchmark until $t = 0.015$. The differences observed later on are mainly due to the chaotic nature of the imposed convection. We have also tested the correction applied when $\chi_{el} > 1$ (Fig. 6f). The differences are small, showing that the correction does not modify the flow significantly.

## Appendix C. Sensitivity to the initial temperature condition

In order to investigate the influence of the temperature initial condition on helium results, we run Model 9 for which the initial condition is similar to the mean temperature profile at $t = 3.5$ billion years in Fig. 2 (i.e. $\theta = 0.8$ from $z = 0$ to $z = 0.25$, and $\theta = 0.2$ from $z = 0.25$ to $z = 1.0$). This initial geotherm also includes thermal boundary layers (87 km thick) located at the top, at the bottom and at the interface between the two layers. The parameters for Model 9 are given in Table 3. Fig. 6h shows the temperature field at elapsed time $t_e = 2.1$ billion years. The denser layer remains stable for at least 2.2 billion years and like for Model 8, the interface between the two layers forms a topography. Fig. 6i represent the R/Ra ratios for our hotspots (35 195 'samples') for the last 150 Myr before $t_e$. The R/Ra spectrum for MORB (not shown here) and for OIB are comparable with those for Model 8 (Fig. 5). This shows that as long as the denser and less degassed layer remains stable, or marginally stable, this configuration will lead to: (1) a sharp spectrum of R/Ra values for ridges because of the efficiency of stirring in the degassed mantle, (2) a large spectrum of R/Ra values for hotspots because of the incorporation of different material with various R/Ra ratios in plumes. This proves that for a stable denser layer, the initial temperature condition does not affect our helium results.

## Appendix D. Effect of random fluctuations on helium results

Since we use a finite number of tracers, random fluctuations may occur. The problem is mainly due to the important differences between helium *masses* (i.e. the concentration of a tracer multiplied by its volume) carried by the different families of tracers in a plume sample. Using 25 tracers/element to model the undegassed layer, the mass of $^3$He represented by an 'undegassed' tracer may be up to $10^4$ times the mass represented by a 'lithospheric' tracer. As a consequence, the presence of an 'undegassed' tracer in a plume sample (due to random fluctuations) may, under certain conditions, boost up the $^3$He concentrations of the sample and thus modify R/Ra. To investigate the effect of random fluctuations, we run Model 10 which differs from Model 9 only by the use of 196 tracers/element to model the undegassed layer, all the other parameters being unchanged. For Model 10 the R/Ra OIB spectrum calculated over the last 150 Myr before the elapsed time $t_e = 2.1$ billion years is shown in Fig. 6j. R/Ra values still range between 0 and 28 but the 'gap' observed in R/Ra distribution (see Figs. 5b and 6i) is now filled because random fluctuations af-

fect less the R/Ra distribution. For ridges, the R/Ra spectrum (not shown here) is unchanged with respect to Model 9, both range between 3 and 9. This test shows that the gap observed in R/Ra spectrum when using 25 tracers/element to model the undegassed layer may be an artifact, and that by using more tracers, the R/Ra OIB spectrum becomes more 'continuous'. However, we remark that the two peaks around R/Ra = 4 and R/Ra = 27 observed in Models 8–10 do not seem to be artificially produced by random fluctuations.

## References

[1] H.P. Bunge, M.A. Richards, C. Lithgow-Bertelloni, J.R. Baumgardner, S.P. Grand, B. Romanowicz, Time scales and heterogeneous structure in geodynamic Earth models, Science 280 (1998) 91–95.

[2] C. Mégnin, B. Romanowicz, The three-dimensional shear velocity structure of the mantle from the inversion of body, surface and higher-mode waveforms, Geophys. J. Int. 143 (2000) 709–728.

[3] M. Ishii, J. Tromp, Normal-mode and free-air gravity constraints on lateral variations in velocity and density of Earth's mantle, Science 285 (1999) 1231–1236.

[4] P.J. Tackley, Three-dimensional simulations of mantle convection with a thermo-chemical CMB boundary layer: D″?, in: M. Gurnis, M.E. Wysession, E. Knittle, B.A. Buffet (Eds.), The Core–Mantle Boundary Region, AGU Geophys. Monogr. 28, 1998, pp. 231–253.

[5] A. Davaille, Simultaneous generation of hotspots and superswells by convection in a heterogeneous planetary mantle, Nature 402 (1999) 756–760.

[6] B.L.N. Kennett, S. Widiyantoro, R.D. van der Hilst, Joint seismic tomography for bulk sound and shear wave speed in the Earth's mantle, J. Geophys. Res. 103 (1998) 12469–12493.

[7] T. Lay, Q. Williams, E.J. Garnero, The core–mantle boundary and deep Earth dynamics, Nature 392 (1998) 461–468.

[8] R.D. van der Hilst, H. Kárason, Compositional heterogeneity in the bottom 1000 kilometers of Earth's mantle: Toward a hybrid convection model, Science 283 (1999) 1885–1888.

[9] A.W. Hofmann, Mantle geochemistry: the message from oceanic volcanism, Nature 385 (1997) 219–229.

[10] N.R.A. Hoffman, D.P. McKenzie, The destruction of geochemical heterogeneities by differential fluid motions during mantle convection, Geophys. J. R. Astron. Soc. 82 (1985) 163–206.

[11] U.R. Christensen, Mixing by time-dependent convection, Earth Planet. Sci. Lett. 95 (1989) 382–394.

[12] P.E. van Keken, C.J. Ballentine, Dynamical models of mantle volatile evolution and the role of phase transitions and temperature-dependent rheology, J. Geophys. Res. 104 (1999) 7137–7151.

[13] U.R. Christensen, A.W. Hofmann, Segregation of subducted oceanic crust in the convecting mantle, J. Geophys. Res. 99 (1994) 19867–19884.

[14] N. Coltice, Y. Ricard, Geochemical observations and one layer mantle convection, Earth Planet. Sci. Lett. 174 (1999) 125–137.

[15] M. Honda, I. McDougall, D.B. Patterson, A. Doulgeris, D.A. Clague, Noble gases in submarine pillow basalt glasses from Loihi and Kilauea, Hawaii: A solar component in the Earth, Geochim. Cosmochim. Acta 57 (1999) 859–874.

[16] E.T. Dixon, M. Honda, I. McDougall, I.H. Campbell, I. Sigurdsson, Preservation of near-solar neon isotopic ratios in Icelandic basalts, Earth Planet. Sci. Lett. 180 (2000) 309–324.

[17] M. Moreira, K. Breddam, J. Curtice, M.D. Kurz, Solar neon in the Icelandic mantle: new evidence for an undegassed lower mantle, Earth Planet. Sci. Lett. 185 (2001) 15–23.

[18] F. Albarède, Time-dependent models of U–T–He and K–Ar evolution and the layering of mantle convection, Chem. Geol. 145 (1998) 413–429.

[19] K.P. Jochum, A.W. Hofmann, E. Ito, H.M. Seufert, W.M. White, K, U and Th in mid-ocean ridge basalt glasses and heat production, K/U and K/Rb in the mantle, Nature 306 (1983) 431–436.

[20] R.K. O'Nions, E.R. Oxburgh, Heat and helium in the Earth, Nature 306 (1983) 429–431.

[21] D.L. Turcotte, W.M. White, Thorium–uranium systematics require layered mantle convection, J. Geophys. Res. 106 (2001) 4265–4276.

[22] L.H. Kellogg, B.H. Hager, R.D. van der Hilst, Compositional stratification in the deep mantle, Science 283 (1999) 1881–1884.

[23] S.D. King, A. Raefsky, B.H. Hager, ConMan: vectorizing a finite element code for incompressible two-dimensional convection in Earth's mantle, Phys. Earth Planet. Inter. 59 (1990) 195–207.

[24] P.E. van Keken, S.D. King, H. Schmeling, U.R. Christensen, D. Neumeister, M.-P. Doin, A comparison of methods for the modeling of thermochemical convection, J. Geophys. Res. 102 (1997) 22477–22495.

[25] D.P. McKenzie, J.M. Roberts, N.O. Weiss, Convection in the Earth's mantle: towards a numerical simulation, J. Fluid Mech. 62 (1974) 465–538.

[26] A. Chopelas, R. Boehler, Thermal expansivity in the lower mantle, J. Geophys. Res. 19 (1992) 1983–1986.

[27] S.B. Jacobsen, G.J. Wasserburg, The mean age of mantle and crustal reservoirs, J. Geophys. Res. 84 (1979) 7411–7427.

[28] D.L. Turcotte, G. Schubert, Geodynamics: Application of Continuum Physics to Geological Problems, Wiley, New York, 1982.

[29] C.L. Harper, S.B. Jacobsen, Noble gazes and Earth's ac-cretion, Science 273 (1996) 1814–1818.

[30] H. Akima, Algorithm 760: rectangular-grid-data surface fitting that has the accuracy of a bicubic polynomial, ACM Trans. Math. Softw. 22 (1996) 357–361.

[31] A.E. Ringwood, T. Irfune, Nature of the 650-km seismic discontinuity: implications for mantle dynamics and dif-ferentiation, Science 331 (1988) 131–136.

[32] A.W. Hofmann, Chemical differentiation of the Earth: the relationship between mantle, continental crust, and oceanic crust, Earth Planet. Sci. Lett. 90 (1988) 297–314.

[33] C.G. Farnetani, Excess temperature of mantle plumes: The role of chemical stratification across D″, Geophys. Res. Lett. 24 (1997) 1583–1586.

[34] U. Hansen, D.A. Yuen, Dynamical influences from ther-mal-chemical instabilities at the core–mantle boundary, Geophys. Res. Lett. 16 (1989) 629–632.

[35] C.G. Farnetani, H. Samuel, Lagrangian structures and stirring in the Earth's mantle, Earth Planet, Sci. Lett. 206 (2003) 335–348.

[36] S. Ferrachat, Y. Ricard, Regular vs. chaotic mantle mix-ing, Earth Planet. Sci. Lett. 155 (1998) 75–86.

[37] Y. Ricard, C. Vigny, Mantle dynamics with induced plate tectonics, J. Geophys. Res. 94 (1989) 17543–17559.

[38] C. Lithgow-Bertelloni, M.A. Richards, Toroidal-poloidal partitioning of plate motions since 120 Ma, Geophys. Res. Lett. 20 (1993) 375–378.

[39] C.W. Gable, R.J. O'Connell, B.J. Travis, Convection in three dimensions with surface plates: generation of toroi-dal flow, J. Geophys. Res. 96 (1991) 8391–8405.

[40] N.L. Montague, L.H. Kellogg, Numerical models of a dense layer at the base of the mantle and implications for the geodynamics of D″, J. Geophys. Res. 105 (2000) 11101–11114.

[41] B. Schott, D.A. Yuen, M. Braun, The influences of com-position-sand temperature-dependent rheology in ther-mal-chemical convection on entrainment of the D″-layer, Phys. Earth Planet. Inter. 129 (2002) 43–65.

[42] K.A. Farley, J.H. Natland, H. Craig, Binary mixing of enriched and undegassed (primitive?) mantle components (He, Sr, Nd, Pb) in Samoan lavas, Earth Planet. Sci. Lett. 111 (1992) 183–199.

[43] M. Moreira, J. Kunz, C. Allègre, Rare gas systematics in popping rock: isotopic and elemental compositions in the upper mantle, Science 279 (1998) 1178–1181.

[44] C.J. Allègre, T. Staudacher, P. Sarda, Rare gaz system-atics: formation of the atmosphere, evolution and struc-ture of the Earth's mantle, Earth Planet. Sci. Lett. 81 (1986) 127–150.